

## RESEARCH ARTICLE

10.1029/2018GC007842

## An Experimental Investigation of the Relative Strength of the Silica Polymorphs Quartz, Coesite, and Stishovite

Simon A. Hunt<sup>1</sup> , Matthew L. Whitaker<sup>2</sup> , Edward Bailey<sup>1,3</sup>, Elisabetta Mariani<sup>4</sup>, Camelia V. Stan<sup>5,6</sup> , and David P. Dobson<sup>1</sup> 

<sup>1</sup>Department of Earth Sciences, University College London, London, UK, <sup>2</sup>Mineral Physics Institute, State University of New York at Stony Brook, Stony Brook, NY, USA, <sup>3</sup>Now at Department of Chemical Engineering, Imperial College London, London, UK, <sup>4</sup>School of Environmental Sciences, Jane Herdman Laboratories, University of Liverpool, Liverpool, UK, <sup>5</sup>Advanced Light Source, Lawrence Berkeley National Laboratory, Berkeley, CA, USA, <sup>6</sup>Now at Lawrence Livermore National Laboratory, Livermore, CA, USA

## Key Points:

- Stishovite is stronger than quartz, coesite, and olivine at  $850 \pm 50$  °C and could be a strong phase in the subducting slab
- The increased strength of stishovite might be related to the change in Si coordination from fourfold to sixfold and its associated density increase
- If generalizable, the increase in Si coordination upon bridgmanite formation explains the viscosity jump around 660 km depth in the Earth

## Supporting Information:

- Supporting Information S1

## Correspondence to:

S. A. Hunt,  
simon.hunt@ucl.ac.uk

## Citation:

Hunt, S. A., Whitaker, M. L., Bailey, E., Mariani, E., Stan, C. V., & Dobson, D. P. (2019). An experimental investigation of the relative strength of the silica polymorphs quartz, coesite, and stishovite. *Geochemistry, Geophysics, Geosystems*, 20, 1975–1989. <https://doi.org/10.1029/2018GC007842>

Received 1 AUG 2018

Accepted 12 MAR 2019

Accepted article online 23 MAR 2019

Published online 23 APR 2019

**Abstract** In this study, quartz, coesite, and stishovite were deformed concurrently with an olivine reference sample at high pressure and  $850 \pm 50$  °C. Olivine deformed with an effective stress exponent ( $n$ ) of  $6.9_{-2.2}^{+3.1}$ , which we interpret to indicate that the Peierls creep deformation mechanism was active in the olivine. Quartz and coesite had very similar strengths and deformed by a mechanism with  $n = 2.8_{-0.9}^{+1.2}$  and  $2.9_{-0.9}^{+1.3}$ , respectively, which are consistent with previous measurements of power law creep in these phases. Stishovite deformed with  $n = 8.1_{-2.7}^{+3.7}$  and was stronger than both olivine and the other silica polymorphs. The high stress exponent of stishovite is greater than that typically observed for power law creep, indicating it is probably (but not certainly) deforming by Peierls creep. The rheology of SiO<sub>2</sub> minerals appears therefore to be strongly affected by the change in silicon coordination and density from fourfold in quartz and coesite to sixfold in stishovite. If the effect of Si coordination can be generalized, the increase in Si coordination (and density) associated with bridgmanite formation may explain the tenfold to 100-fold viscosity increase around 660 km depth in the Earth.

### 1. Introduction

The principal phases of pure silica (SiO<sub>2</sub>), quartz, coesite, and stishovite are important minerals in the Earth and are a microcosm of the diverse crystal structures found in silicate minerals. Quartz is the second most abundant phase in the Earth's continental crust (after feldspar) and transforms to coesite above ~3 GPa (Bohlen & Boettcher, 1982), around 90 km depth in the Earth. The presence of coesite is a defining feature of ultrahigh-pressure metamorphic terrains and evidence that continental crust can be subducted deeper than 90 km before being returned to the surface (e.g., Chopin, 2003). In the Earth, stishovite is stable above ~9 GPa, ~275 km depth (Ono et al., 2017; Zhang et al., 1993), and is a significant component of basaltic oceanic crust deeper than ~400 km (Perrillat et al., 2006). The decomposition products of aluminous stishovite have been found as inclusions in ultradeep diamonds (Bulanova et al., 2010; Thomson et al., 2014; Zedgenizov et al., 2015).

The low-pressure (<9 GPa) silica polymorphs (quartz, coesite, tridymite, and cristobalite) as well as low-pressure silica glass are formed from different arrangements of SiO<sub>4</sub> tetrahedra. The tetrahedral units, within which a silicon atom is surrounded by four equally spaced oxygen atoms, form the structural backbone for the panoply of silicate minerals present in the Earth's rocky crust and upper mantle (e.g., Deer et al., 1992; Liebau, 1985). Under pressure, the tetrahedral unit is replaced by octahedral, six-coordinated silicon (SiO<sub>6</sub>), which exhibits a much smaller number of crystal structures and generally higher density. The high-pressure structures are typified by rutile-structured stishovite above ~10 GPa, CaCl<sub>2</sub>-structured SiO<sub>2</sub> above ~40 GPa, and α-PbO<sub>2</sub>-structured seifertite above ~120 GPa (e.g., Grocholski et al., 2013; Murakami et al., 2003), all of which contain corner-sharing SiO<sub>6</sub> octahedra. Very few minerals have both four- and six-coordinated silicon (Finger & Hazen, 1991). Silicon coordinated with an odd number of oxygens is not found in natural minerals, although it has been shown to exist in high-pressure silica glasses and melts (e.g., Wu et al., 2012); metastable high-pressure phases (Finkelstein et al., 2015a, 2015ab); and, very rarely, in synthetic crystalline solids such as CaSi<sub>2</sub>O<sub>5</sub> (Angel et al., 1996).

The increase of silicon coordination upon the formation of stishovite ( $\rho = 4.3$  g/cm<sup>3</sup>) is reflected in it having a significantly greater density than either quartz ( $\rho = 2.6$  g/cm<sup>3</sup>) or coesite ( $\rho = 2.9$  g/cm<sup>3</sup>). The change in Si

coordination appears to have a significant effect on material properties. The rheology of quartz has been measured in many studies (Blacic & Christie, 1984; Gleason & Tullis, 1995; Jaoul et al., 1984; Kronenberg & Tullis, 1984; Xiao et al., 2002). Both Ingrin and Gillet (1986) and Langenhorst and Poirier (2002) interpreted Transmission Electron Microscope observations of coesite to say that it is less deformable than quartz, yet it is still relatively weak under ultrahigh-pressure metamorphic conditions (Renner et al., 2001). In contrast, polycrystalline stishovite is among the strongest known oxides with sufficiently high fracture toughness and shear modulus that it is classified as a “superhard” material (Léger et al., 1996). Stishovite supports extremely high differential stresses during compression in the diamond anvil cell (Singh et al., 2012), and while it has been deformed to reasonable strain (Kaercher et al., 2015; Texier & Cordier, 2006), its rheology has not been measured. The high hardness of stishovite is likely to persist at high temperatures because of its extremely slow silicon diffusion (Shatskiy et al., 2010; Xu et al., 2017).

The rheology of stishovite and its associated Si-coordination change therefore have potentially important implications for the Earth. Its abundance in subducted slabs is perhaps sufficient for it to influence slab rheology. However, the relative strength of the silica polymorphs, both among themselves and relative to other mantle phases, is unknown. Here we report the results of deformation experiments on quartz, coesite, and stishovite and discuss their broader implications for the deep Earth.

## 2. Experimental Method

The results reported here are further analyses of three experiments, initially reported by Hunt et al. (2014), that were performed during commissioning of the DT-Cup on the side-station beamline X17B2ss at the NSLS. The DT-Cup is a modified split-cylinder six to eight multianvil capable of controlled strain rate deformation experiments (Hunt et al., 2014; Hunt & Dobson, 2017). The  $\langle 111 \rangle$  axes of the inner cubic anvils are aligned with the compression direction of the loading frame. The “top” and “bottom” cubic anvils are replaced with hexagonal cross section anvils, the inner end of which has the same profile as that of the cubic anvils they replace. These anvils are driven by secondary hydraulic actuators, thus enabling deformation.

The six cubic and two hexagonal anvils compress a cell assembly consisting of a 7 mm chrome-doped MgO octahedron within which is a 4.7 mm-long, 1.2 mm inner diameter, 200  $\mu\text{m}$  wall thickness cylindrical graphite furnace, which is enclosed at the ends by 0.5 mm-thick steel end caps. Samples of San Carlos olivine powder with a 20- to 50- $\mu\text{m}$  grain size and either finely ground amorphous silica glass or quartz powder (see Table 1), with an initial length of  $\sim 0.8$  mm, were loaded into the furnace. Outside the samples were 0.6-mm-long corundum pistons, with the remaining space filled with crushable alumina. The samples were separated from each other and the pistons by 25- $\mu\text{m}$ -thick platinum disks, which also acted as strain markers. The thermocouple was inserted through the octahedron in a radial configuration with respect to the furnace. A thin layer of alumina cement was used to insulate the thermocouple hot junction from the furnace. Illustrations of the cell were presented in Hunt et al. (2014).

Each experiment was pressurized over 2–3 hr and annealed at a thermocouple temperature of 800  $^{\circ}\text{C}$  for between 2 and 4 hr prior to deformation. Because the thermocouple is outside of the furnace, the sample temperature will have been greater than the thermocouple measurement. Subsequent tests, using the same experimental cell design, with a thermocouple both inside and outside of the furnace have shown that the temperature inside the furnace is always hotter than the external thermocouple reading. The difference in temperature is as high as 10%, but it is highly dependent on the position of the external thermocouple junction relative to the outer edge of the furnace because this is where the largest thermal gradients are present in the cell (Hernlund et al., 2006). We therefore expect our sample temperatures to be between  $850 \pm 50$   $^{\circ}\text{C}$ .

The assembly was deformed by advancing the differential pistons at a fixed rate; two or three different deformation rates were used in each experiment. X-radiography images were acquired every 60 s during deformation, with an exposure time of 5 s, using a fluorescent yttrium-aluminum garnet crystal scintillator and a visible light camera. Diffraction patterns were acquired from the samples and corundum piston before deformation and toward the end of each deformation-rate step, using a MAR345 image plate with an exposure time of 300 s. The image plate parameters and energy of the monochromatic X-ray beam were calibrated using a reference  $\text{CeO}_2$  diffraction pattern taken before the experiments started. Example radiographs and diffraction patterns are shown in Hunt et al. (2014). After deformation the experiments were quenched

**Table 1**  
*Experimental Conditions, Differential Stresses, Strain Rates and Recovered Grain Sizes Measured in Both the Olivine and SiO<sub>2</sub> Samples*

Experiment	SiO <sub>2</sub> phase		Force kN	Pressure during deformation GPa <sup>b</sup>	Differential stress GPa	Strain rate		Strain rate ratio SiO <sub>2</sub> /olivine	Total strain accumulated by both samples at steady state <sup>a</sup> %	Recovered grain size (diameter)	
	Loaded	Made				Olivine (s <sup>-1</sup> )	SiO <sub>2</sub> (s <sup>-1</sup> )			Olivine (μm)	Silica (μm)
SiO_40	Quartz	Quartz	113	~3	— —	3.1(2) × 10 <sup>-6</sup> 3.3(3) × 10 <sup>-5</sup>	4.3(3) × 10 <sup>-6</sup> 1.1(1) × 10 <sup>-5</sup>	1.40(15) 0.33(4)	8.1 28.1	—	—
SiO_38	Glass	Coesite	390	~2	0.51(6) 0.93(6) 0.81(6)	9.0(11) × 10 <sup>-7</sup> 1.3(1) × 10 <sup>-5</sup> 3.9(3) × 10 <sup>-5</sup>	2.1(2) × 10 <sup>-6</sup> 8.2(5) × 10 <sup>-6</sup> 8.4(7) × 10 <sup>-6</sup>	2.30(33) 0.64(5) 0.22(2)	1.0 12.8 10.2	3.5	2.3
SiO_39	Glass	Stishovite	946	~9.5	0.73(12) 1.15(11) 1.25(12)	5.4(4) × 10 <sup>-7</sup> 1.6(3) × 10 <sup>-6</sup> 6.8(4) × 10 <sup>-6</sup>	1.8(3) × 10 <sup>-7</sup> 5.4(18) × 10 <sup>-7</sup> 3.4(3) × 10 <sup>-6</sup>	0.33(7) 0.34(13) 0.50(6)	2.5 3.1 4.3	3.7	1.8

*Note.* The numbers in parentheses are one standard error of the least significant digit of the value. All the data were collected at ~850 ± 50 °C. The reported grain diameters are the mean area of the grains in the electron backscatter diffraction maps (Figure 5) converted to a diameter assuming circular grains.

<sup>a</sup>The sum of the strains here is less than the total strains reported previously by Hunt et al. (2014) because any transient deformation arising after the change in strain rate has been discarded. <sup>b</sup>Pressures as reported by Hunt et al. (2014); errors are of order 1.5 GPa.

and decompressed. Both the end load and the differential load were reduced over the same time period to try and prevent damage to the samples.

The recovered samples were mounted in resin and polished for analysis in the X500 CrystalProbe field emission gun Scanning Electron Microscope at the University of Liverpool. The final polish was a chemo-mechanical polish using 0.03 μm colloidal silica in an alkaline solution. Samples were coated with a thin carbon layer before electron backscatter diffraction (EBSD) patterns were obtained using 20 kV accelerating voltage, 35 nA beam current, and 25 mm working distance, with 0.5 μm grid spacing. These were automatically indexed using Oxford Instrument's AZtec software package (Prior et al., 2009). The three expected silica phases were listed as possible options during indexing, as well as olivine, enstatite, alumina, and platinum. Indexing of the coesite in experiment SiO\_38 was challenging; the sample deformation was heterogeneous, and only the less distorted Kikuchi patterns, away from the most strained areas, could be indexed successfully. High residual strains and amorphization of the samples also hampered EBSD analyses. Due to similar challenges, samples in SiO\_40 (quartz and olivine) were therefore analyzed by Laue diffraction on beamline 12.3.2 at the Advanced Light Source (Kunz et al., 2009). The samples were placed with the polished surface at 45° geometry with respect to the X-ray beam, which was focused to 2 × 2 μm. Patterns were collected in both Laue mode (energy range 5–24 keV) and in monochromatic mode (10 keV) onto a Pilatus M1 detector positioned at 90° relative to the incident X-ray beam. The detector position was calibrated using an unstrained Si single crystal sample prior to measurements being performed. Data were processed using XMAS (Tamura, 2014). For the Laue (white beam) measurements, the footprint of the beam onto the sample is 2 × 3 μm, with a penetration depth of about 100 μm; therefore, the diffracting volume is on the order of 600 μm<sup>3</sup>. The footprint is larger (5 × 4 μm) for monochromatic experiments, but the penetration depth is smaller.

The recovered samples were too fragmented for it to be possible to measure their water content. Water solubility in pure silica phases at low temperature is small (Gerretsen et al., 1989; Koch-Müller et al., 2001), but the samples are unlikely to be dry because no steps were taken to control water content before or during the experiments. Even with fired cell parts and encapsulated samples, samples in solid-media apparatus experiments absorb water (e.g., Rubie et al., 1993), presumably gained from the atmosphere during preparation. Since all samples were prepared in the same environment, following the same procedures and all experiments were performed using the same cell design, we can tentatively assume that similar quantities of water would have been available for hydration of nominally dry samples in each experiment.

### 3. Data Analysis

Strain in the samples was determined from the X-radiographs. The position of the platinum marker foils in the images was tracked using the cross-correlation method described in previous work (Hunt et al., 2012; Li

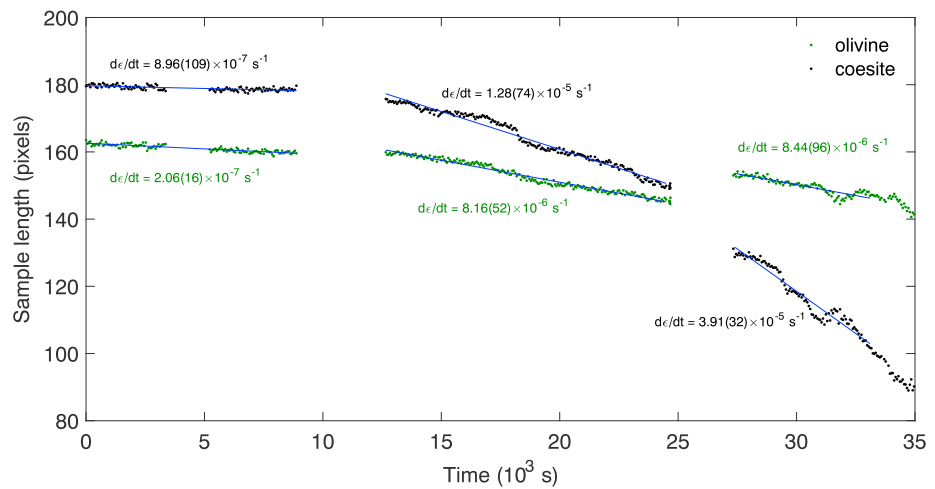


**Figure 1.** Strain and stress during experiment SiO<sub>38</sub>. Black and green dots are the measured lengths of the olivine and coesite samples, respectively. Blue lines are the fits for the strain rates, which are denoted by the text; the numbers in parentheses are one standard error of the least significant digit. The strain rates were changed during the gaps in the data, when X-ray diffraction patterns were also acquired.

et al., 2003). Sample strains were calculated from the change in length of each sample (Figure 1). Strain rates were calculated as the ordinary least squares fit of a first degree polynomial to the strain after discarding any transient conditions arising from the change in imposed shortening rate. The strain rate error is the standard error on the fit accounting for the assumed  $\pm 10$  pixel error in the length of the samples.

Stress in the samples was calculated from the diffraction patterns. Not using low-scattering X-ray windows along the X-ray beam path resulted in the sample diffraction peaks (olivine and SiO<sub>2</sub>) being overlaid by diffraction from the pyrophyllite gaskets and MgO pressure medium. Integrating around the entire Debye rings made the diffraction peaks from the silica sufficiently distinct for the phase of silica to be identified. Hunt et al. (2014) calculated the pressure in these experiments by integration of the corundum diffraction patterns and fitting the corundum peaks using Multifit (Merkel & Hilairret, 2015). The unit-cell volume was calculated from the fitted peaks and the pressure determined using the equation of state of Dubrovinsky et al. (1998;  $K = 258[2]$ ,  $K' = 4.88$ ,  $\alpha_T = 2.6[2] \times 10^{-5} + 1.81[9] \times 10^{-9} T - 0.67[6]/T^2$ ). The measured pressure dropped significantly during annealing and crystallization of the coesite and stishovite samples. In the coesite experiment the pressure apparently dropped from  $\sim 8.8$  to  $\sim 2$  GPa. This is common during synthesis of coesite because of the large volume change between silica glass and coesite. During deformation of the coesite, the actual pressure is probably  $> 3$  GPa because no significant quartz was observed in the recovered sample.

Calculating differential stress was more difficult and was not done in our previous paper. Further interrogation of the diffraction patterns has enabled us to extract stress estimates from some of the diffraction data. To estimate differential stress, the diffraction peaks were integrated into  $20^\circ$  wide azimuthal segments using Fit2D (Hammersley et al., 1995, 1996). The first three corundum diffraction peaks (the [012], [104], and [110] peaks) were complete and distinguishable from the pyrophyllite background. The presence of multiple broad and ill-defined pyrophyllite peaks prevented the utilization of automated diffraction peak fitting software (e.g., Multifit, Merkel & Hilairret, 2015). Therefore, each integrated diffraction segment was interpolated with a cubic spline and the maxima in the location of the corundum peaks selected as the peaks' centroids.

Differential stresses were calculated from the variations in peak position with azimuth (Figure 2) using Polydefix (Merkel & Hilairret, 2015) and the Al<sub>2</sub>O<sub>3</sub> bulk ( $K$ ) and shear ( $G$ ) moduli of Higo et al., (2018;  $K = 251.2$  GPa,  $K' = 4.21$ ,  $dK/dT = -0.025$  GPa/K,  $G = 164.1$  GPa,  $G' = 1.59$ ,  $dG/dT = -0.021$  GPa/K) and thermal expansion of Dubrovinsky et al. (1998). For each experiment the Bulk and Shear moduli at the conditions of the experiment were calculated and used as fixed values in the Polydefix calculation. The corundum, from which the stress is calculated, is not in the hot spot of the furnace and is close to the

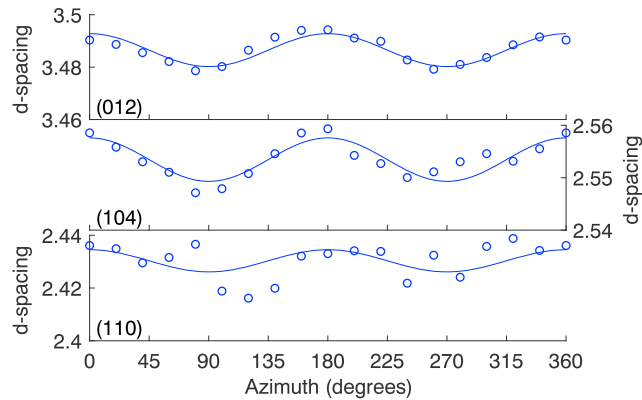


**Figure 2.** Variation of  $\text{Al}_2\text{O}_3$  d-spacing with azimuth during at the highest strain rate during experiment SiO\_38. Top, middle, and bottom are the (012), (104), and (110) diffraction peaks, respectively. Circles are the measured d-spacings, and the line is the fit produced in polydefix (Merkel & Hilaret, 2015).

tungsten carbide anvils. It is therefore at a significantly lower temperature than the sample. The temperature in the alumina was assumed to be 400 °C because of the thermal gradient in the cell. Changing the assumed temperature or pressure had little effect on the calculated differential stresses, and variations were significantly smaller than the error in the stress.

This approach to picking peaks worked well for experiment SiO\_38 (coesite) in which each of the diffraction peaks followed the expected  $\cos^2$  relationship with azimuth (e.g., Singh et al., 1998) and gave acceptable (i.e., positive and finite) stresses for the corundum (Figure 2). For SiO\_39 (the stishovite experiment), only the (110) corundum peak gave acceptable stress values. No consistent stresses could be calculated for the quartz experiment (SiO\_40) because the corundum diffraction peaks in this experiment were less distinct than for the other two experiments. The pressure calculated for the experiments using this method does not correspond to the pressure calculated previously by Hunt et al. (2014). This is probably due to the overlaps between the corundum and pyrophyllite diffraction peaks. Within each experiment though, there is little change between diffraction patterns in the size and shape of the overlapping peaks; therefore, the relative magnitudes of the stress in each experiment are considered to be internally consistent.

The relationship between stress and strain rate in a material is controlled by the active deformation mechanisms. The strain rate ( $\dot{\epsilon}$ ) of a sample is the sum of strain rates of all active, independent mechanisms:

$$\dot{\epsilon}_{\text{total}} = \dot{\epsilon}_{\text{power-law}} + \dot{\epsilon}_{\text{diffusion creep}} + \dot{\epsilon}_{\text{GBS}} + \dot{\epsilon}_{\text{Peierls creep}}, \quad (1)$$

where GBS indicates grain boundary sliding. In each of these deformation mechanisms the strain rate is a function of differential stress and temperature among other factors.

At high temperatures, the general form of a thermally activated flow law (e.g., power law or diffusion creep) is

$$\dot{\epsilon} = A \frac{\sigma^n}{d^p} f_{\text{H}_2\text{O}}^r \exp\left(-\frac{E^* + PV^*}{RT}\right), \quad (2)$$

where  $\dot{\epsilon}$  is the strain rate,  $\sigma$  the differential stress,  $n$  is the stress exponent,  $d$  is the grain size,  $p$  the grain-size exponent,  $f_{\text{H}_2\text{O}}$  is the water fugacity with exponent  $r$ ,  $E^*$  is the activation enthalpy of the thermally driven process,  $V^*$  the activation volume,  $P$  is the pressure,  $R$  is the gas constant,  $T$  the temperature, and  $A$  is the constant of proportionality. Very often,  $Q$  is used as the activation energy and is equal to  $E^* + PV^*$  (see Hirth & Kohlstedt, 2003).

The stress exponent ( $n$ ) is the power coefficient relating the differential stress ( $\sigma$ ) to the strain rate ( $\dot{\epsilon}$ ). The value of  $n$  (and those of the other parameters) varies to reflect a given deformation mechanism. Diffusion creep mechanisms have  $n \sim 1$  and are grain-size sensitive ( $p > 0$ ), while for power law creep in olivine

$n > 3.5$  and  $p \sim 0$ . An intermediate mechanism, which is observed to occur at the transition between dislocation creep and diffusion creep, is dislocation accommodated grain boundary sliding, sometimes known as DisGBS (Warren & Hirth, 2006).

In solids deforming at low temperatures, plasticity, or Peierls creep, is generally the dominant mechanism. This deformation mechanism has a stress-dependent activation energy for creep and a flow law with the form

$$\dot{\epsilon} = A\sigma^2 \exp\left(-\frac{Q}{RT} \left[1 - \left(\frac{\sigma}{\tau}\right)^p\right]^q\right), \quad (3)$$

where  $Q$  is the thermal activation energy at zero stress,  $\tau$  is the Peierls stress, and  $p$  and  $q$  are exponents with limits  $0 \leq p \leq 1$  and  $1 \leq q \leq 2$ , respectively (Frost & Ashby, 1982). The stress exponent here is not a simple function of stress and an *effective* stress exponent calculated from this flow law will be both (a) strain rate dependent and (b) greater than the typical values for power law creep.

We determined the stress exponent in our samples using a total least squares (Markovsky & Van Huffel, 2007; Van Huffel & Vandewalle, 1989) fit to the  $\ln(\sigma) - \ln(\dot{\epsilon})$  data (listed in Table 1). For olivine we also determined  $V^*$  from the two experiments that gave good differential stresses again using a total least squares fit. The standard errors on the  $\sigma$  and  $\dot{\epsilon}$  are symmetrical in linear space and therefore asymmetrical in log-log space. To account for the asymmetrical errors, a Monte Carlo method (e.g., Anderson, 1976) was used to calculate the errors in  $n$  and  $V^*$ . Monte Carlo error propagation is widely used and returns answers consistent with algebraic answers for weighted fitting problems in which the algebra is known. In the Monte Carlo calculation here,  $10^5$  independent models were generated; in each model the stresses and strain rates were drawn from a random distribution of the values and their associated Gaussian errors. The pressure and temperature in each model were also selected using their estimated errors of 1.5 GPa and 50 °C, respectively. The reported values of  $n$  and  $V^*$  (Table 2) are the mean and standard deviation of the array of calculated values. Because the distribution of  $n$  values is lognormal, the value of  $n$  determined from the values in Table 1 is somewhat different to that returned by the Monte Carlo calculation.

The overlapping peaks in the diffraction patterns prevented the determination of differential stresses for experiment SiO\_40 (quartz deformation). To enable the calculation of a stress exponent for quartz and to validate interpretation of the coesite and stishovite results, differential stresses were calculated using previously published olivine flow laws (listed in Table 3). These differential stresses were then combined with the silica phase strain rates to predict the stress exponent.

The differential stresses were calculated for the measured olivine strain rates at the pressure and temperature conditions of the experiments. The pressures in the models were assumed to be those reported in Table 1 with an error of 1.5 GPa, except for experiment SiO\_38 where the pressure was assumed to be 3 GPa. The temperatures were taken to be  $850 \pm 50$  °C, and, where required, the grain size was taken to be the values reported in Table 1. For SiO\_40 no grain size was measured, so the mean of the values from the other experiments was used. The grain size has only a small effect on the calculated stress exponents because the stress exponent ( $n$ ) is independent of grain size ( $d$ ; equation (2)). As intracrystalline water content could not be determined, it was assumed that samples were dry. The stress exponents of the silica phases are the gradients of a total least squares fit of a straight line to the olivine flow-law-derived differential stresses and the silica strain rates.

Errors in the stress exponents were calculated from the flow-law parameters and strain rate uncertainties using a similar Monte Carlo calculation to that used earlier. In this Monte Carlo calculation,  $10^5$  sets of differential stresses were calculated from each flow law, accounting for the uncertainties in the reported flow-law parameters, pressure, temperature, and our measured olivine strain rates. After discarding models that had negative differential stresses, the computed differential stresses and the measured silica strain rates were used to determine a stress exponent. The reported values of the stress exponents in Table 2 are the mean and standard deviation of the  $10^5$  modeled stress exponents. For most of the models the distribution of values is approximately Gaussian and the most probable value almost the same as the mean. The models for which a Gaussian distribution is not a good approximation for are the Peierls creep flow law of Raterron et al. (2004) and flow laws that combine multiple deformation mechanisms; histograms of the calculated stress exponents are shown in Figures S1–S14 in the supporting information.

**Table 2**  
Calculated Stress Exponents and Activation Volumes

Experiment	$n$	Olivine		Silica polymorphs	
		$V^*$ (cm <sup>3</sup> /mol)	$n_{\text{quartz}}$	$n_{\text{coesite}}$	$n_{\text{stishovite}}$
SiO_38	7.4 <sup>+2.5</sup> <sub>-1.9</sub>			2.7 <sup>+0.8</sup> <sub>-0.6</sub>	
SiO_39	5.2 <sup>+3.2</sup> <sub>-2.0</sub>				6.6 <sup>+4.9</sup> <sub>-2.8</sub>
Combined	6.9 <sup>+3.1</sup> <sub>-2.2</sub>	4.6 <sup>+2.2</sup> <sub>-1.5</sub>	2.8 <sup>+1.2<sup>a</sup></sup> <sub>-0.9</sub>	2.9 <sup>+1.3<sup>a</sup></sup> <sub>-0.9</sub>	8.1 <sup>+3.7<sup>a</sup></sup> <sub>-2.7</sub>

*Note.* The values are the mean and standard deviation of the lognormal distribution to values returned by the Monte Carlo estimation; the stress exponents calculated from the unweighted values in Table 1 differ from these values by less than 0.3, except for Stishovite which is different by 0.7.

<sup>a</sup>Calculated from the linear scaling relationship between stress exponents in Table 3 and combined stress exponent of olivine; see text for details.

For the Peierls creep models, we also calculated the effective olivine stress exponent by the same total least squares method.

The calculated differential stresses in some of these models have formal error greater than half a log unit (Figures S1–S14, part a), which derives primarily from poorly constrained pre-exponential factors (such as  $A$ ; equation (1)). The large stress errors do not significantly affect the error on the silica polymorphs' stress exponents because  $n$  is a small number compared to the differential stresses. The grain size and water fugacity used in the calculations do not affect the calculated stress exponent, only the stresses.

## 4. Results

### 4.1. Rheological Data

The phase of silica identified in each experiment along with the measured strain rates and diffraction-derived differential stresses are presented in Table 1 and the stress-strain rate relationship for the coesite and stishovite samples is shown in Figure 1a. No reasonable stresses could be calculated for the quartz

**Table 3**  
Stress Exponents Calculated From Each Candidate Olivine Flow Law

Flow-law	Deformation mechanism	Olivine		Silica stress exponent ( $n$ )			Representative flow-law stress.
		Stress exponent ( $n_{\text{olivine}}$ ) <sup>a</sup>	Effective stress exponent	Quartz	Coesite	Stishovite	Log <sub>10</sub> (MPa)
Faul and Jackson (2007)	Diffusion Creep	1.37(6)		0.6(1)	0.6(1)	1.7(2)	-1.7(12)
Hansen et al. (2011)	Grain Boundary Sliding	2.9(3)		1.2(2)	1.2(2)	3.5(6)	3.6(6)
Nishihara et al. (2014)	Grain Boundary Sliding	3		1.2(2)	1.3(1)	3.7(5)	4.2(10)
Karato and Jung (2003)	Power Law Creep	3.0(1)		1.2(2)	1.3(1)	3.7(5)	5.0(6)
Wang et al. (2010) <sup>b</sup>	Grain Boundary Sliding	3.5(1)		1.4(2)	1.5(1)	4.3(6)	1.4(1)
Nishihara et al. (2014)	Power Law Creep	3.5		1.4(2)	1.5(1)	4.3(5)	4.4(9)
Chopra and Paterson (1984)	Power Law Creep	3.60(22)		1.4(2)	1.5(2)	4.4(7)	4.0(5)
Kranjc et al. (2016)	Peierls Creep		6.3(1) <sup>c</sup>	2.6(3) <sup>c</sup>	2.7(2) <sup>c</sup>	7.1(10) <sup>c</sup>	2.4 <sup>c</sup>
Raterron et al. (2004)	Pearls Creep		9.2(56)	3.6(18)	3.7(19)	10.0(56)	2.5(5)
Demouchy et al. (2013)	Peierls Creep		9.5(28)	3.8(11)	4.0(11)	11.0(33)	2.9(3)
Mei et al. (2010)	Peierls Creep		13.1(26)	5.3(12)	5.6(12)	15.4(36)	3.3(1)
Evans and Goetze (1979)	Peierls Creep		26.9(19) <sup>c</sup>	10.6(14) <sup>c</sup>	11.6(10) <sup>c</sup>	32.6(39) <sup>c</sup>	3.6 <sup>c</sup>
Hirth and Kohlstedt (2003)	Combined (power law and diffusion creep)		3.2(15)	1.3(4)	1.3(4)	3.7(12)	4.5(8)
Nishihara et al. (2014)	Combined (power law and diffusion creep)		4.8(34)	1.7(4)	1.8(4)	5.1(14)	4.0(11)

*Note.* The distributions of the silica stress exponents are shown in Figures S1–S14. The numbers in parentheses are the standard error on the least significant figure. The representative differential stresses in the last column are those for the slowest strain rate point in the coesite experiment ( $\dot{\epsilon}_{\text{olivine}}=8.96(96)\times 10^{-7}$ /s;  $P = 3$  GPa;  $T = 850$  °C).

<sup>a</sup>Values in this column are reported in previous studies; all other values are calculated as part of this study. <sup>b</sup>Using the flow-law parameters reported by Hansen et al. (2011). <sup>c</sup>Errors on these numbers are nonexistent or significantly less than the others because no errors were associated with the flow-law coefficients in the source manuscripts.

sample, so it is not includable in this plot. Despite the fact that there is significant scatter in the data, it is evident in Figure 1a that at similar stresses stishovite is stronger than coesite, deforming over an order of magnitude slower.

Direct comparison of the strength of quartz with the higher pressure silica phases is only possible via the measured olivine strain rates. Figure 1b shows that in our experiments the quartz and coesite deformed at very similar strain rates relative to olivine. Both quartz and coesite have higher strain rates than olivine for  $\dot{\epsilon}_{\text{olivine}} \lesssim 5 \times 10^{-6}/\text{s}$  and lower strain rate for  $\dot{\epsilon}_{\text{olivine}} > 5 \times 10^{-6}/\text{s}$ . Thus, their strength may be comparable to that of olivine, and both phases must have a stress exponent smaller than that of olivine. On the other hand, quartz and coesite are weaker (i.e., deform at faster rates) than stishovite under all the conditions explored in our experiments. The strain rates in stishovite are lower than those in olivine, and the ratio,  $\dot{\epsilon}_{\text{SiO}_2} / \dot{\epsilon}_{\text{olivine}}$ , increases with olivine strain rate (Table 1). The ratio for stishovite varies between 0.33 and 0.5, indicating that in our experiment stishovite is two to three times stronger than olivine.

The relative strength of the silica phases measured here is at an unknown water fugacity. All the silica phases have been shown to take small amounts of water into their structures (Gerretsen et al., 1989; Mosenfelder, 2000; Pawley et al., 1993). Quartz weakens significantly under hydrous conditions (e.g., Blacic & Christie, 1984), and olivine has been shown to weaken by a factor of between 1.3 and 2.5 between nominally dry and wet conditions (Girard et al., 2013; Mackwell et al., 1985). The effect of water fugacity on the rheology of coesite and stishovite is unknown. The equivalent treatment of all the samples and experimental assemblies means it is reasonable to assume a similar and relatively low water activity in all the experiments. However, it should be noted that if the effect of water on viscosity of the silica polymorphs is very different and our experiments are unexpectedly wet, then our results might not be representative.

For our coesite and stishovite experiments, stress exponents could be calculated directly from the differential stresses (Figure 3a). The values reported in Table 2 are the mean and standard deviation of the lognormal distribution of bootstrapped  $n$  values; the stress exponents calculated from the values in Table 1 differ from these values by less than 0.3, except for stishovite which is different by 0.7. From experiment SiO\_38, the  $n_{\text{coesite}}$  derived here agrees, within error, with Renner et al. (2001)'s value of  $3 \pm 1$ , but the corresponding olivine stress exponent is very high for power law creep. Conversely, the  $n_{\text{olivine}}$  from SiO\_39 is within error of previously published values for power law creep (e.g., Table 2). The  $n_{\text{olivine}}$  values from the two experiments are within error of each other. Combining the two experiments (Figure 4) gives  $n_{\text{olivine}} = 6.9^{+3.1}_{-2.2}$ , a value that is significantly higher than the widely accepted power law stress exponent of 3 to 3.5. Assuming the pressure experiments SiO\_38 and SiO\_39 was 9.5 and 3 GPa, respectively, the activation volume is  $4.6^{+2.2}_{-1.5} \text{ cm}^3/\text{mole}$ , within the range of previously published high pressure values (Kaboli et al., 2017; Nishihara et al., 2014). However, the validity of activation volume is dependent on the deformation mechanisms in the two olivine sample being the same.

## 4.2. Recovered Microstructures

Despite numerous attempts, it was not possible to index the quartz or olivine in experiment SiO\_40 by EBSD. Laue microdiffraction from the sample showed that both the quartz and olivine grain sizes are much smaller than the beam size ( $2 \times 2 \mu\text{m}$  FWHM,  $\sim 600 \mu\text{m}^3$  diffraction volume) and have highly distorted crystal lattices. Subsequent powder diffraction indicated that both quartz and olivine are crystalline with significant peak broadening, indicating a small grain size and/or extremely high dislocation densities (Figures 5a and 5b). Quartz appears to show no preferred orientation, whereas slight lattice preferred orientation may be observed in olivine.

The olivine sample deformed concurrently with coesite developed a strong deformation fabric and significant reduction from the loaded 20- to 50  $\mu\text{m}$  diameter grain size (Figure 5c). In the olivine sample there are large, distorted grains with subgrains and large populations of smaller grains with a crystallographic preferred orientation (CPO). These samples were deformed to high strains (>50%), and their microstructures show evidence for dynamic recrystallization (subgrain rotation recrystallization with minor grain boundary migration—Figure 5d) that is characteristic of a dislocation-mitigated deformation mechanism (e.g., Bystricky et al., 2000). The interiors of large grains in the coesite sample are well indexed by EBSD (Figure 5c). Some grains exhibit internal lattice distortions that indicate the presence of dislocations.

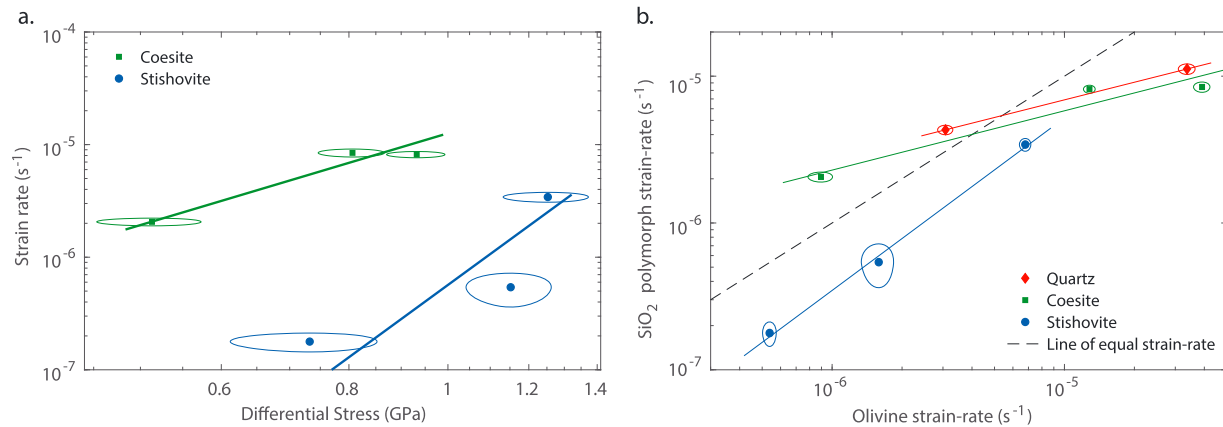


**Figure 3.** (a) Differential stress versus silica polymorph strain rate and (b)  $\text{SiO}_2$  polymorph strain rate versus olivine strain rate. Solid lines are linear fit to the data. The ellipsoids delimit the strain rates' standard errors, and in (b) the black dashed line is the 1:1 equal strain rate line.

Samples in SiO\_39 (stishovite + olivine) were deformed to significantly less total strain than that imposed on the lower pressure phases (Table 1). Therefore, fabrics in these samples are less well developed. The maximum grain size observed in the olivine (Figure 5f) is of order  $20 \mu\text{m}$ , and the mean diameter is  $\sim 3.7 \mu\text{m}$ , which is a reduction of the initial 20- to  $50 \mu\text{m}$ -diameter grain-size. Additionally, both the olivine and stishovite phases show disequilibrium grain boundaries, with many quadruple junctions and highly serrated grain boundaries. The relative lack of lattice distortion within grains points to a low dislocation density, consistent with the smaller total strain in these samples. The total strain in both samples for the stishovite experiment (SiO\_39) is  $\sim 10\%$  while the total strain in the quartz (SiO\_40) and coesite (SiO\_39) experiments was closer to 60 %. Thus, the samples in the lower-pressure experiments have significantly more strain in which to develop strong fabrics and CPO.

The numerically smaller olivine stress exponent calculated for the stishovite experiment (Table 2) might be due to different deformation mechanism activity in the olivine sample, the difference in CPO and total strains. However, we have no evidence for this here beyond the stress-exponent measurements and the measured olivine stress exponents are within error of each other. Thus, it is reasonable to assume that to first order the olivine samples have the same deformation mechanism and the calculated activation volume for creep is valid within this assumption.

#### 4.3. Flow-Law Modeling

Stress exponents for the silica phases were predicted from a suite of previously published olivine flow laws. The flow laws used and the stress exponents calculated are listed in Table 3; the stress-strain rate relationship for each flow law and the histogram of the Monte Carlo-derived stress exponents are in Figures S1-S14.

The predicted stress exponent in the  $\text{SiO}_2$  phases scales linearly with  $n_{\text{olivine}}$  (Table 3). Olivine flow laws with a stress exponent close to 1 (e.g., Faul & Jackson, 2007) give unrealistically low-stress exponents for both the quartz and coesite ( $n \sim 0.6$ ) and differential stresses of order 20 Pa (Table 3). Olivine flow laws with  $2.9 < n_{\text{olivine}} < 3.5$  (equation (2), dislocation creep with or without grain boundary sliding) predict stress exponents for quartz and coesite between 1.2 and 1.5 and, for stishovite, between 3.7 and 4.4. The calculated differential stresses for these mechanisms are all greater than  $\sim 3 \text{ GPa}$ , apart from Wang et al. (2010), where the stresses are  $< 50 \text{ MPa}$  (Table 3). The two flow laws that combined power law creep and diffusion creep (Hirth & Kohlstedt, 2003; Nishihara et al., 2014) have bimodal distributions for  $n$ , with maxima that reflect the dominance of either diffusion or power law creeps (Figures S13 and S14). For

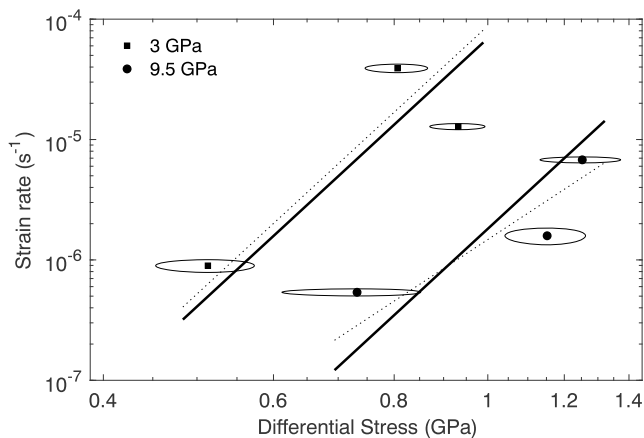


**Figure 4.** Stress versus strain rate plot for the olivine in experiments SiO\_38 and SiO\_39. Ellipsoids denote the errors on the values. Heavy lines are the fit to all the data, and the dashed lines are the fit to each data set individually.

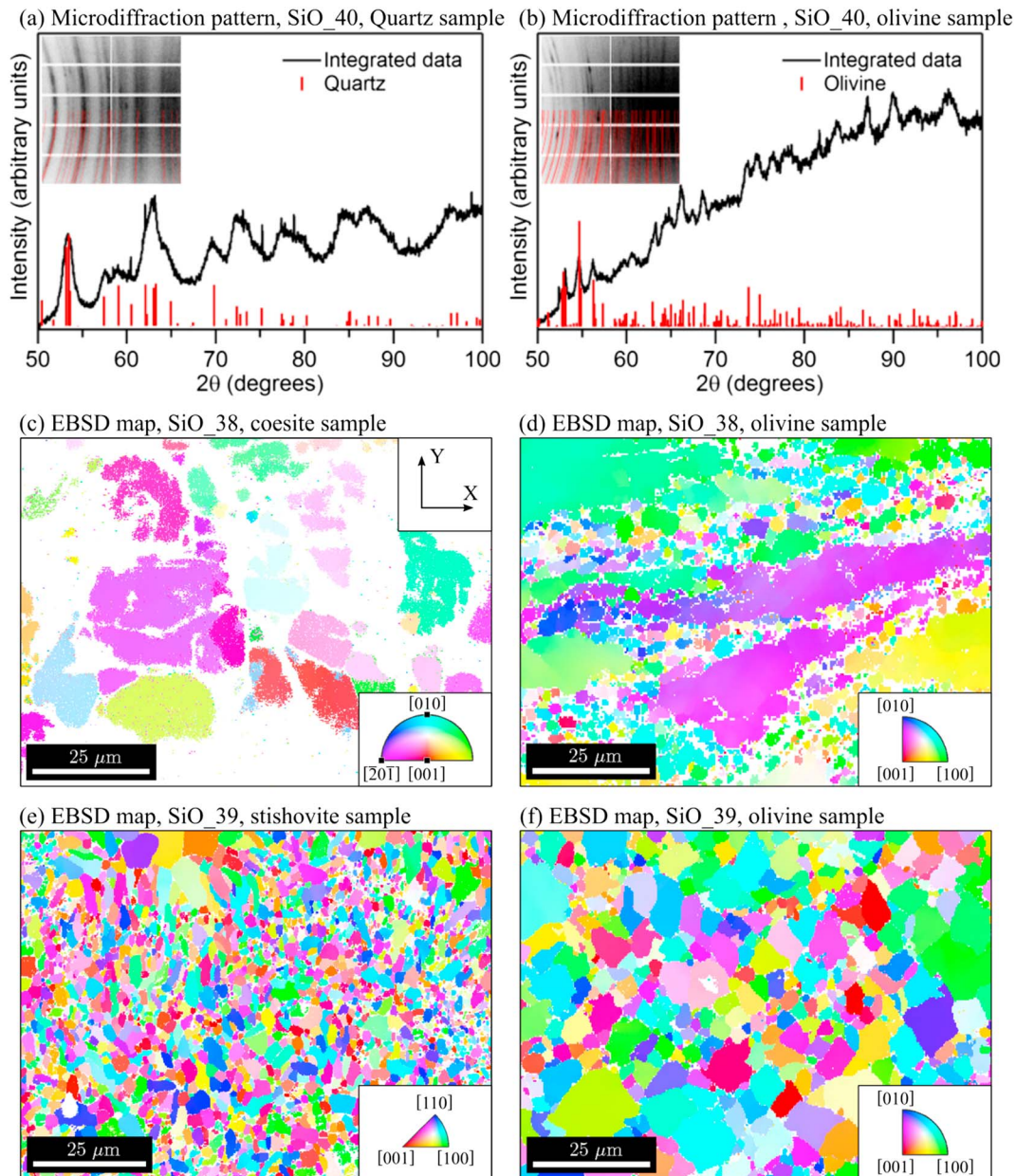


**Figure 5.** Integrated microdiffraction patterns or inverse pole figure electron backscatter diffraction (EBSD) maps, plotted with respect to *Y* (stress direction), of the recovered samples. (a and b) Quartz deformation experiment, (c and d) coesite deformation experiment, and (e and f) stishovite deformation experiment. (a), (c), and (e) are silica samples, and (b), (d), and (f) are the olivine samples. (a and b) Diffraction patterns collected at 10 keV (wavelength = 1.2398 Å) and radially integrated with 0.01° resolution in 2θ; red lines: Predicted location of quartz or olivine peaks. Inset: raw data. Inserts to (c)–(f): color-coded legends for inverse pole figure maps (EBSD reference frame is reported in c). The mean grain diameters are reported in Table 1.

both flow laws, the Monte Carlo simulations prefer the power law creep mechanism and, like the power law flow laws, predict very high differential stresses. Assuming a Peierls mechanism for olivine (equation (3); e.g., Raterron et al., 2004), with an exponential stress dependence, gives much larger effective stress exponents ( $6 > n > 27$ ). The Peierls mechanisms with effective stress exponents between 3 and 9 have differential stress on the order of ~250 MPa and the predicted differential stresses increase with  $n$ . All Peierls deformation mechanisms give high stress dependency for stishovite ( $7 > n > 33$ ).

In Table 3 the silica polymorph stress exponents scale linearly with  $n_{\text{olivine}}$ . Using these relationships, and our measured value of  $n_{\text{olivine}} = 6.9^{+3.1}_{-2.2}$  (Table 2), we get  $n_{\text{quartz}} = 2.8^{+1.2}_{-0.9}$ ,  $n_{\text{coesite}} = 2.9^{+1.3}_{-0.9}$ , and  $n_{\text{stishovite}} = 8.1^{+3.7}_{-2.7}$ .

## 5. Conclusions

In this study quartz and coesite have very similar strengths, and both are weaker than stishovite (Figure 3b). The strength of stishovite increases relative to the other silica phases and olivine with reductions in strain rate. The unmeasured water concentration of the samples in this study mean that the absolute strength of the phases analyzed is poorly constrained here. Unless, however, stishovite undergoes significantly more hydrolytic weakening than quartz, it must be stronger than quartz at mantle strain rates. The ability to use the data here as a guide to strength contrast between the silica phases in the mantle depends on the deformation mechanisms active in this study.

For the olivine in this study, we measured  $n_{\text{olivine}} = 6.9^{+3.1}_{-2.2}$  and  $V^* = 4.6^{+2.2}_{-1.5}$  cm<sup>3</sup>/mole. The stress exponents for the individual experiments are within error of this combined value (Table 2). Although it has large errors, this stress exponent is within one standard error of the effective stress exponents estimated for the flow laws of Kranjc et al. (2016), Raterron et al. (2004), and Demouchy et al. (2013) and is significantly greater than the measured stress exponents for power law creep (Table 3; e.g., Kaboli et al., 2017; Nishihara et al., 2014). The differential stresses predicted by the Peierls creep flow laws with  $n < 10$  are similar in magnitude to our measured stresses, unlike those for the diffusion creep and most of the power laws, which are unreasonably high and low, respectively (Table 3), at the conditions of our experiments (Table 1). The olivine in these experiments is therefore deforming by Peierls creep.

No activation volume has been previously reported for Peierls creep in olivine. The activation volume measured here is within the range of previously measured values for deformation by diffusion and power law creep (0–15 cm<sup>3</sup>/mol; e.g., Kaboli et al., 2017; Nishihara et al., 2014).

Microstructural evidence from the olivine supports our choice of dislocation-mitigated deformation mechanisms but does not uniquely distinguish between Peierls or power law creep. It must be noted that in this study we have no evidence in support of, or against, the activity of grain boundary sliding during dislocation creep.

The stress exponents for coesite calculated directly from the data ( $2.7^{+0.8}_{-0.6}$ ) and using the combined olivine stress exponent ( $2.9^{+1.3}_{-0.9}$ ) are within error of each other and of the only other previously published stress exponent for power law creep in coesite,  $3 \pm 1$  (Renner et al., 2001). This supports the interpretation of Peierls creep as the active deformation mechanism in the olivine.

No direct measurement of the stress exponent in quartz was possible, but an exponent of  $2.8^{+1.2}_{-0.9}$  was estimated from the combined olivine stress exponent and the stress exponent scaling relations apparent in the modeling (Table 3). Although subject to more uncertainty than a directly measured value, it is close to the value of  $n_{\text{quartz}} = 2.97$  for quartz deforming by “dislocation creep, with some contribution from grain-boundary sliding” (Rutter & Brodie, 2004) and is consistent with previous measurements for power law creep in quartz ( $n_{\text{quartz}} = 2$ , Shelton & Tullis, 1981;  $n_{\text{quartz}} = 2.3 \pm 0.1$  and  $2.4 \pm 0.4$ , Jaoul et al., 1984). In quartz, the transition temperature between Peierls and power law creep is around 600 °C (Evans & Goetze, 1979); therefore, power law creep is expected to be the active deformation mechanism in this experiment.

Similarly to the coesite, the directly measured ( $n_{\text{stishovite}} = 6.6^{+4.9}_{-2.8}$ ) and scaled ( $n_{\text{stishovite}} = 8.1^{+3.7}_{-2.7}$ ) stress exponents for stishovite are within error of each other. They are higher than typically reported for power law creep exponents in silicate minerals and greater than the  $n = 5$  stress exponent seen during dislocation climb controlled creep in some metals. It is most likely therefore (but not certain) that stishovite is deforming by Peierls creep.

In which case, the transition temperature between Peierls and power law creep is greater in stishovite than in quartz and coesite. Peierls creep, or plasticity, is dominated by gliding of dislocations without any contribution from diffusion controlled dislocation climb, which is the controlling factor in power law creep. The absence of diffusion control in Peierls creep is reflected in the relative temperature independence of the deformation mechanism. The probable higher temperature transition between deformation mechanisms in stishovite is therefore consistent with the low diffusion rates in stishovite and faster diffusion rates in quartz and coesite. The preference for Peierls over power law creep implies that power law creep is much stronger in stishovite under the conditions of these experiments, again consistent with slow diffusion

rates. At some temperature higher than those here ( $850 \pm 50$  °C), the dominant deformation mechanism will change to power law creep, weakening the stishovite somewhat. But because of the very slow diffusion rate of Si, stishovite will remain stronger than quartz and coesite.

Stishovite has a smaller unit cell than either quartz or coesite, and the typical slip-system Burgers vector is also shorter (e.g., Idrissi et al., 2008; Texier & Cordier, 2006). The higher strength of stishovite indicates therefore that the dislocation mobility cannot be significantly greater in stishovite than in quartz or coesite and is probably much lower. This is consistent with very slow silicon and oxygen diffusion observed in stishovite (Xu et al., 2017). All three silica phases studied here are tectosilicates, so, unlike in olivine, Si-O bonds must be broken and reformed for motion of dislocations to occur in the crystals. The Si-O electrostatic bond strength in stishovite is less than that in quartz and coesite (Gibbs et al., 2008, 2009), but silicon and oxygen diffusion in octahedral stishovite is significantly slower than in tetrahedral phases. The increase in silicon coordination and the higher density of stishovite may therefore generate geometric difficulties that retard diffusion and impede the dislocation mobility in stishovite relative to the other phases.

As with the pure SiO<sub>2</sub> system, a pressure-induced change in silicon coordination and concurrent increase in density is seen in the (Mg,Fe)O-CaO-SiO<sub>2</sub> system, which dominates the chemistry of the Earth's mantle. Above ~20 GPa Ca(Si,Ti)O<sub>3</sub> perovskite becomes the main carrier of calcium, with a framework of fully corner-sharing (Si,Ti)O<sub>6</sub> silica octahedra. Above ~23 GPa the magnesium silicate components of the mantle ([Mg,Fe]SiO<sub>3</sub> and [Mg,Fe]<sub>2</sub>SiO<sub>4</sub>) transform into (Mg,Fe)SiO<sub>3</sub> bridgmanite ± (Mg,Fe)O; here the silicate is an orthorhombic perovskite (GdFeO<sub>3</sub>-type structure) that forms ~70 vol.% of the Earth's lower mantle between 25 and 110 GPa. At greater depths bridgmanite transforms into the CaIrO<sub>3</sub>-structured "post-perovskite" phase, which also contains octahedrally coordinated silica units, arranged as corner- and edge-sharing sheets (Murakami et al., 2004; Oganov & Ono, 2004).

Like stishovite, bridgmanite is both dense ( $\rho = 4.1$  g/cm<sup>3</sup>; Sugahara et al., 2006) and shows extremely slow diffusion of both Mg and Si cations (Ammann et al., 2010; Dobson et al., 2008; Holzapfel et al., 2003; Yamazaki et al., 2000). High temperature deformation experiments on bridgmanite, with and without ferro-periclase, shows that bridgmanite is very resistant to deformation (Girard et al., 2016; Tsujino et al., 2016) and that it supports larger differential stresses than less dense, lower-pressure phases (Chen et al., 2002). Our qualitative experience of crushing bridgmanite samples for X-ray powder diffraction studies also suggests that it is significantly harder than the other polymorphs of MgSiO<sub>3</sub>. Geophysical evidence implies that the lower mantle has between 10 and 100 times higher viscosity than the upper mantle. Due to the depth at which it occurs, the viscosity contrast is widely associated with the formation of bridgmanite and may therefore be associated with the formation of octahedrally coordinated silicon in bridgmanite.

However, the formation of bridgmanite convolves other effects with the increase in silicon coordination, for example, changes in cation coordination and network connectivity of the silica units in the magnesium silicate crystal structures. Cation coordination and valence play a role in the strength of phases, for example, the substitution of  $2Al^{3+}$  by  $Si^{4+} + Mg^{2+}$  in pyrope garnet weakens the mineral (Hunt et al., 2010) as does the substitution of  $Fe^{2+}$  into forsterite (Bollinger et al., 2015). In general substitution of multivalent and less strongly charged cations reduces the strength of minerals. The formation of bridgmanite from Mg<sub>2</sub>SiO<sub>4</sub> involves a change in the Mg-Si and Si-O ratio, which may also affect the strength. This ratio change is not present in the MgSiO<sub>3</sub> system, where stiff bridgmanite is formed from majorite, which is weak (Hunt et al., 2010). Like the silica polymorphs, bridgmanite is a tectosilicate with a three-dimensional structure of interlocking silica units, and the formation of bridgmanite increases the network of the silica units. Postperovskite, which not a tectosilicate, is weak (Ammann et al., 2010; Hunt et al., 2009), but this appears to be related to enhanced diffusivity of Mg and Si and not uniquely weak glide planes. There are though no obvious general relationships between the strength of silicates and their crystal symmetry or the network coordination of their silica units.

These structural and cation ambiguities are not present in the silica polymorphs, all of which consist of fully corner-sharing SiO<sub>4</sub> or SiO<sub>6</sub> frameworks and have the same silicon-oxygen ratio. The present study shows for the first time that stishovite is significantly stronger than either quartz or coesite. We have argued that silica coordination (and an associated density increase) may play a significant role in the strength of the silicate phases. By analogy, the increase in Si coordination between MgSiO<sub>3</sub> and Mg<sub>2</sub>SiO<sub>4</sub> lower pressure

polymorphs and bridgmanite may cause the increased strength of bridgmanite and thus explain the tenfold to 100-fold increase in viscosity around 660 km depth in the Earth.

#### Acknowledgments

S. A. H. (NE/H016309/1 and NE/L006898/1), D. P. D. (NE/K002902/1), and E. M. (NE/L007363/1) thank the Natural Environment Research Council (NERC) for funding. Use of the National Synchrotron Light Source, Brookhaven National Laboratory, was supported by the U.S. Department of Energy, Office of Science, Office of Basic Energy Sciences, under Contract No. DE-AC02-98CH10886. Use of the X17B2 beamline was supported by COMPRES, the Consortium for Materials Properties Research in Earth Sciences under NSF Cooperative Agreement EAR 10-43050 and by the Mineral Physics Institute, Stony Brook University. This research used resources of the Advanced Light Source, which is a DOE Office of Science User Facility under contract No. DE-AC02-05CH11231. We thank the four reviewers and editor for their comments, which resulted in a much improved manuscript. The data used in this study are available online (<https://dx.doi.org/10.5285/c35acc1b-88a4-4215-b4c2-df50d2bf3ba4>).

#### References

- Ammann, M. W., Brodholt, J. P., Wookey, J., & Dobson, D. P. (2010). First-principles constraints on diffusion in lower-mantle minerals and a weak  $D''$  layer. *Nature*, *465*(7297), 462–465. <https://doi.org/10.1038/nature09052>
- Anderson, G. M. (1976). Error propagation by the Monte Carlo method in geochemical calculations. *Geochimica et Cosmochimica Acta*, *40*(12), 1533–1538. [https://doi.org/10.1016/0016-7037\(76\)90092-2](https://doi.org/10.1016/0016-7037(76)90092-2)
- Angel, R. J., Ross, N. L., Seifert, F., & Fliervoet, T. F. (1996). Structural characterization of pentacoordinate silicon in a calcium silicate. *Nature*, *384*(6608), 441–444. <https://doi.org/10.1038/384441a0>
- Blacic, J. D., & Christie, J. M. (1984). Plasticity and hydrolytic weakening of quartz single crystals. *Journal of Geophysical Research*, *89*(B6), 4223–4239. <https://doi.org/10.1029/JB089iB06p04223>
- Bohlen, S. R., & Boettcher, A. L. (1982). The quartz  $\rightleftharpoons$  coesite transformation: A precise determination and the effects of other components. *Journal of Geophysical Research*, *87*(B8), 7073–7078. <https://doi.org/10.1029/JB087iB08p07073>
- Bollinger, C., Merkel, S., Cordier, P., & Raterron, P. (2015). Deformation of forsterite polycrystals at mantle pressure: Comparison with Fe-bearing olivine and the effect of iron on its plasticity. *Physics of the Earth and Planetary Interiors*, *240*, 95–104. <https://doi.org/10.1016/j.pepi.2014.12.002>
- Bulanova, G. P., Walter, M. J., Smith, C. B., Kohn, S. C., Armstrong, L. S., Blundy, J., & Gobbo, L. (2010). Mineral inclusions in sublithospheric diamonds from Collier 4 kimberlite pipe, Juina, Brazil: Subducted protoliths, carbonated melts and primary kimberlite magmatism. *Contributions to Mineralogy and Petrology*, *160*(4), 489–510. <https://doi.org/10.1007/s00410-010-0490-6>
- Bystricky, M., Kunze, K., Burlini, L., & Burg, J.-P. (2000). High shear strain of olivine aggregates: Rheological and seismic consequences. *Science*, *290*(5496), 1564–1567. <https://doi.org/10.1126/science.290.5496.1564>
- Chen, J., Weidner, D. J., & Vaughan, M. T. (2002). The strength of Mg(0.9)Fe(0.1)SiO<sub>3</sub> perovskite at high pressure and temperature. *Nature*, *419*(6909), 824–826. <https://doi.org/10.1038/nature01130>
- Chopin, C. (2003). Ultrahigh-pressure metamorphism: Tracing continental crust into the mantle. *Earth and Planetary Science Letters*, *212*, 1–14. [https://doi.org/10.1016/S0012-821X\(03\)00261-9](https://doi.org/10.1016/S0012-821X(03)00261-9)
- Chopra, P. N., & Paterson, M. S. (1984). The role of water in the deformation of dunite. *Journal of Geophysical Research*, *89*(B9), 7861–7876. <https://doi.org/10.1029/JB089iB09p07861>
- Deer, W. A., Howie, R. A., & Zussman, J. (1992). *An Introduction to the Rock-Forming Minerals*. New York: Longman, Harlow/Wiley.
- Demouchy, S., Tommasi, A., Boffa Ballaran, T., & Cordier, P. (2013). Low strength of earth's uppermost mantle inferred from tri-axial deformation experiments on dry olivine crystals. *Physics of the Earth and Planetary Interiors*, *220*, 37–49. <https://doi.org/10.1016/j.pepi.2013.04.008>
- Dobson, D. P., Dohmen, R., & Wiedenbeck, M. (2008). Self-diffusion of oxygen and silicon in MgSiO<sub>3</sub> perovskite. *Earth and Planetary Science Letters*, *270*(1–2), 125–129. <https://doi.org/10.1016/j.epsl.2008.03.029>
- Dubrovin, L. S., Saxena, S. K., & Lazor, P. (1998). High-pressure and high-temperature in situ X-ray diffraction study of iron and corundum to 68 GPa using an internally heated diamond anvil cell. *Physics and Chemistry of Minerals*, *25*(6), 434–441. <https://doi.org/10.1007/s002690050133>
- Evans, B., & Goetze, C. (1979). The temperature variation of hardness of olivine and its implication for polycrystalline yield stress. *Journal of Geophysical Research*, *84*(B10), 5505. <https://doi.org/10.1029/JB084iB10p05505>
- Faul, U. H., & Jackson, I. (2007). Diffusion creep of dry, melt-free olivine. *Journal of Geophysical Research*, *112*, B04204. <https://doi.org/10.1029/2006JB004586>
- Finger, L. W., & Hazen, R. M. (1991). Crystal chemistry of six-coordinated silicon: A key to understanding the Earth's deep interior. *Acta Crystallographica Section B*, *47*(5), 561–580. <https://doi.org/10.1107/S0108768191004214>
- Finkelstein, G. J., Dera, P. K., & Duffy, T. S. (2015a). High-pressure phases of cordierite from single-crystal X-ray diffraction to 15 GPa. *American Mineralogist*, *100*(8–9), 1821–1833. <https://doi.org/10.2138/am-2015-5073>
- Finkelstein, G. J., Dera, P. K., & Duffy, T. S. (2015b). Phase transitions in orthopyroxene (En 90) to 49 GPa from single-crystal X-ray diffraction. *Physics of the Earth and Planetary Interiors*, *244*, 78–86. <https://doi.org/10.1016/j.pepi.2014.10.009>
- Frost, H. J., & Ashby, M. F. (1982). *Deformation-mechanism maps: The Plasticity and Creep of Metals and Ceramics*. Pergamon Press.
- Gerretsen, J., Paterson, M. S., & McLaren, A. C. (1989). The uptake and solubility of water in quartz at elevated pressure and temperature. *Physics and Chemistry of Minerals*, *16*(4), 334–342. <https://doi.org/10.1007/BF00199553>
- Gibbs, G. V., Downs, R. T., Cox, D. F., Ross, N. L., Prewitt, C. T., Rosso, K. M., et al. (2008). Bonded interactions and the crystal chemistry of minerals: A review. *Zeitschrift Für Kristallographie - Crystalline Materials*, *223*(01–02), 01–40. <https://doi.org/10.1524/zkri.2008.0002>
- Gibbs, G. V., Wallace, A. F., Cox, D. F., Downs, R. T., Ross, N. L., & Rosso, K. M. (2009). Bonded interactions in silica polymorphs, silicates, and siloxane molecules. *American Mineralogist*, *94*(8–9), 1085–1102. <https://doi.org/10.2138/am.2009.3215>
- Girard, J., Amulule, G., Farla, R., Mohiuddin, A., & Karato, S. (2016). Shear deformation of bridgmanite and magnesiowüstite aggregates at lower mantle conditions. *Science*, *351*(6269), 144–147. <https://doi.org/10.1126/science.aad3113>
- Girard, J., Chen, J., Raterron, P., & Holyoke, C. W. (2013). Hydrolytic weakening of olivine at mantle pressure: Evidence of [100](010) slip system softening from single-crystal deformation experiments. *Physics of the Earth and Planetary Interiors*, *216*, 12–20. <https://doi.org/10.1016/j.pepi.2012.10.009>
- Gleason, G. C., & Tullis, J. (1995). A flow law for dislocation creep of quartz aggregates determined with the molten salt cell. *Tectonophysics*, *247*(1–4), 1–23. [https://doi.org/10.1016/0040-1951\(95\)00011-B](https://doi.org/10.1016/0040-1951(95)00011-B)
- Grocholski, B., Shim, S.-H., & Prakapenka, V. B. (2013). Stability, metastability, and elastic properties of a dense silica polymorph, seifertite. *Journal of Geophysical Research: Solid Earth*, *118*, 4745–4757. <https://doi.org/10.1002/jgrb.50360>
- Hammersley, A. P., Svensson, S. O., Hanfland, M., Fitch, A. N., & Hausermann, D. (1996). Two-dimensional detector software: From real detector to idealised image or two-theta scan. *High Pressure Research*, *14*(4–6), 235–248. <https://doi.org/10.1080/08957959608201408>
- Hammersley, A. P., Svensson, S. O., Thompson, A., Graafsma, H., Kvick, Å., & Moy, J. P. (1995). Calibration and correction of distortions in two-dimensional detector systems a. *Review of Scientific Instruments*, *66*(3), 2729–2733. <https://doi.org/10.1063/1.1145618>
- Hansen, L. N., Zimmerman, M. E., & Kohlstedt, D. L. (2011). Grain boundary sliding in San Carlos olivine: Flow law parameters and crystallographic-preferred orientation. *Journal of Geophysical Research*, *116*, B08201. <https://doi.org/10.1029/2011JB008220>

- Hernlund, J., Leinenweber, K., Locke, D., & Tyburczy, J. A. (2006). A numerical model for steady-state temperature distributions in solid-medium high-pressure cell assemblies. *American Mineralogist*, *91*(2–3), 295–305. <https://doi.org/10.2138/am.2006.1938>
- Higo, Y., Irifune, T., & Funakoshi, K. (2018). Simultaneous high-pressure high-temperature elastic velocity measurement system up to 27 GPa and 1873 K using ultrasonic and synchrotron X-ray techniques. *Review of Scientific Instruments*, *89*(1), 014501. <https://doi.org/10.1063/1.4993121>
- Hirth, G., & Kohlstedt, D. L. (2003). Rheology of the upper mantle and the mantle wedge: A view from the experimentalists upper mantle. We first analyze experimental data to provide a critical review of flow. In *Inside the subduction factory, Geophysical Monograph Series* (Vol. 138, pp. 83–105). Washington, DC: American Geophysical Union. <https://doi.org/10.1029/138GM06>
- Holzappel, C., Rubie, D. C., Mackwell, S., & Frost, D. J. (2003). Effect of pressure on Fe-Mg interdiffusion in (Fe<sub>x</sub>Mg<sub>1-x</sub>)O, ferropericlasite. *Physics of the Earth and Planetary Interiors*, *139*(1–2), 21–34. [https://doi.org/10.1016/S0031-9201\(03\)00142-0](https://doi.org/10.1016/S0031-9201(03)00142-0)
- Hunt, S. A., Davies, D. R., Walker, A. M., McCormack, R. J., Wills, A. S., Dobson, D. P., & Li, L. (2012). On the increase in thermal diffusivity caused by the perovskite to post-perovskite phase transition and its implications for mantle dynamics. *Earth and Planetary Science Letters*, *319*–320, 96–103. <https://doi.org/10.1016/j.epsl.2011.12.009>
- Hunt, S. A., & Dobson, D. P. (2017). Modified anvil design for improved reliability in DT-Cup experiments. *The Review of Scientific Instruments*, *88*(12), 126106. <https://doi.org/10.1063/1.5005885>
- Hunt, S. A., Dobson, D. P., Li, L., Weidner, D. J., & Brodholt, J. P. (2010). Relative strength of the pyrope-majorite solid solution and the flow-law of majorite containing garnets. *Physics of the Earth and Planetary Interiors*, *179*(1–2), 87–95. <https://doi.org/10.1016/j.pepi.2009.12.001>
- Hunt, S. A., Weidner, D. J., Li, L., Wang, L., Walte, N., Brodholt, J. P., & Dobson, D. P. (2009). Weakening of CaIrO<sub>3</sub> during the perovskite-post perovskite transformation. *Nature Geoscience*, *2*(11), 794–797. <https://doi.org/10.1038/NGEO663>
- Hunt, S. A., Weidner, D. J., McCormack, R. J., Whitaker, M. L., Bailey, E., Li, L., et al. (2014). Deformation T-Cup: A new multi-anvil apparatus for controlled strain-rate deformation experiments at pressures above 18 GPa. *Review of Scientific Instruments*, *85*(8), 085103. <https://doi.org/10.1063/1.4891338>
- Idrissi, H., Cordier, P., Jacob, D., & Walte, N. (2008). Dislocations and plasticity of experimentally deformed coesite. *European Journal of Mineralogy*, *20*(4), 665–671. <https://doi.org/10.1127/0935-1221/2008/0020-1849>
- Ingrin, J., & Gillet, P. (1986). TEM investigation of the crystal microstructures in a quartz-coesite assemblage of the western alps. *Physics and Chemistry of Minerals*, *13*(5), 325–330. <https://doi.org/10.1007/BF00308349>
- Jaoul, O., Tullis, J., & Kronenberg, A. (1984). The effect of varying water contents on the creep behavior of Heavitree quartzite. *Journal of Geophysical Research*, *89*(B6), 4298–4312. <https://doi.org/10.1029/JB089iB06p04298>
- Kaboli, S., Burnley, P. C., Xia, G., & Green, H. W. (2017). Pressure dependence of creep in forsterite olivine: Comparison of measurements from the D-DIA and Griggs apparatus. *Geophysical Research Letters*, *44*, 10,939–10,947. <https://doi.org/10.1002/2017GL075177>
- Kaercher, P. M., Zepeda-Alarcon, E., Prakapenka, V. B., Kanitpanyacharoen, W., Smith, J. S., Sinogeikin, S., & Wenk, H.-R. (2015). Preferred orientation in experimentally deformed stishovite: Implications for deformation mechanisms. *Physics and Chemistry of Minerals*, *42*(4), 275–285. <https://doi.org/10.1007/s00269-014-0718-5>
- Karato, S.-I., & Jung, H. (2003). Effects of pressure on high-temperature dislocation creep in olivine. *Philosophical Magazine*, *83*(3), 401–414. <https://doi.org/10.1080/0141861021000025829>
- Koch-Müller, M., Fei, Y., Hauri, E., & Liu, Z. (2001). Location and quantitative analysis of OH in coesite. *Physics and Chemistry of Minerals*, *28*(10), 693–705. <https://doi.org/10.1007/s002690100195>
- Kranjc, K., Rouse, Z., Flores, K. M., & Skemer, P. (2016). Low-temperature plastic rheology of olivine determined by nanoindentation. *Geophysical Research Letters*, *43*, 176–184. <https://doi.org/10.1002/2015GL065837>
- Kronenberg, A. K., & Tullis, J. (1984). Flow strengths of quartz aggregates: Grain size and pressure effects due to hydrolytic weakening. *Journal of Geophysical Research*, *89*(B6), 4281–4297. <https://doi.org/10.1029/JB089iB06p04281>
- Kunz, M., Tamura, N., Chen, K., MacDowell, A. A., Celestre, R. S., Church, M. M., et al. (2009). A dedicated superbend x-ray microdiffraction beamline for materials, geo-, and environmental sciences at the advanced light source. *Review of Scientific Instruments*, *80*(3), 035108. <https://doi.org/10.1063/1.3096295>
- Langenhorst, F., & Poirier, J. (2002). Transmission electron microscopy of coesite inclusions in the Dora Maira high-pressure metamorphic pyrope-quartzite. *Earth and Planetary Science Letters*, *203*(3–4), 793–803. [https://doi.org/10.1016/S0012-821X\(02\)00949-4](https://doi.org/10.1016/S0012-821X(02)00949-4)
- Léger, J. M., Haines, J., Schmidt, M., Petitet, J. P., Pereira, A. S., & da Jornada, J. A. H. (1996). Discovery of hardest known oxide. *Nature*. <https://doi.org/10.1038/383401a0>
- Li, L., Raterron, P., Weidner, D. J., & Chen, J. (2003). Olivine flow mechanisms at 8 GPa. *Physics of the Earth and Planetary Interiors*, *138*(2), 113–129. [https://doi.org/10.1016/S0031-9201\(03\)00065-7](https://doi.org/10.1016/S0031-9201(03)00065-7)
- Liebau, F. (1985). *Structural chemistry of silicates*. Berlin, Heidelberg: Springer. <https://doi.org/10.1007/978-3-642-50076-3>
- Mackwell, S. J., Kohlstedt, D. L., & Paterson, M. S. (1985). The role of water in the deformation of olivine single crystals. *Journal of Geophysical Research*, *90*(B13), 11319. <https://doi.org/10.1029/JB090iB13p11319>
- Markovsky, I., & Van Huffel, S. (2007). Overview of total least-squares methods. *Signal Processing*, *87*(10), 2283–2302. <https://doi.org/10.1016/j.sigpro.2007.04.004>
- Mei, S., Suzuki, A. M., Kohlstedt, D. L., Dixon, N. A., & Durham, W. B. (2010). Experimental constraints on the strength of the lithospheric mantle. *Journal of Geophysical Research*, *115*, B08204. <https://doi.org/10.1029/2009JB006873>
- Merkel, S., & Hilaret, N. (2015). Multifit/Polydefix: A framework for the analysis of polycrystal deformation using X-rays. *Journal of Applied Crystallography*, *48*(4), 1307–1313. <https://doi.org/10.1107/S1600576715010390>
- Mosenfelder, J. L. (2000). Pressure dependence of hydroxyl solubility in coesite. *Physics and Chemistry of Minerals*, *27*(9), 610–617. <https://doi.org/10.1007/s002690000105>
- Murakami, M., Hirose, K., Ono, S., & Ohishi, Y. (2003). Stability of CaCl<sub>2</sub>-type and  $\alpha$ -PbO<sub>2</sub>-type SiO<sub>2</sub> at high pressure and temperature determined by in-situ X-ray measurements. *Geophysical Research Letters*, *30*(5), 1207. <https://doi.org/10.1029/2002GL016722>
- Murakami, M., Hirose, K., Sata, K., Nagayoshi, K., & Ohishi, Y. (2004). Post-perovskite phase transition in MgSiO<sub>3</sub>. *Science*, *304*(5672), 855–858. <https://doi.org/10.1126/science.1095932>
- Nishihara, Y., Ohuchi, T., Kawazoe, T., Spengler, D., Tasaka, M., Kikegawa, T., et al. (2014). Rheology of fine-grained forsterite aggregate at deep upper mantle conditions. *Journal of Geophysical Research: Solid Earth*, *119*, 253–273. <https://doi.org/10.1002/2013JB010473>
- Oganov, A. R., & Ono, S. (2004). Theoretical and experimental evidence for a post-perovskite phase of MgSiO<sub>3</sub> in Earth's D'' layer. *Nature*, *430*(6998), 445–448. <https://doi.org/10.1038/nature02701>

- Ono, S., Kikegawa, T., Higo, Y., & Tange, Y. (2017). Precise determination of the phase boundary between coesite and stishovite in SiO<sub>2</sub>. *Physics of the Earth and Planetary Interiors*, 264, 1–6. <https://doi.org/10.1016/j.pepi.2017.01.003>
- Pawley, A. R., McMillan, P. F., & Holloway, J. R. (1993). Hydrogen in stishovite, with implications for mantle water content. *Science*, 261(5124), 1024–1026. <https://doi.org/10.1126/science.261.5124.1024>
- Perrillat, J.-P., Ricolleau, A., Daniel, L., Fiquet, G., Mezouar, M., Guignot, N., & Cardon, H. (2006). Phase transformations of subducted basaltic crust in the uppermost lower mantle. *Physics of the Earth and Planetary Interiors*, 157(1–2), 139–149. <https://doi.org/10.1016/j.pepi.2006.04.001>
- Prior, D. J., Mariani, E., & Wheeler, J. (2009). EBSD in the Earth sciences: Applications, common practice, and challenges. In *Electron Backscatter Diffraction in Materials Science* (pp. 345–360). Boston, MA: Springer. [https://doi.org/10.1007/978-0-387-88136-2\\_26](https://doi.org/10.1007/978-0-387-88136-2_26)
- Raterron, P., Wu, Y., Weidner, D. J., & Chen, J. (2004). Low-temperature olivine rheology at high pressure. *Physics of the Earth and Planetary Interiors*, 145(1–4), 149–159. <https://doi.org/10.1016/j.pepi.2004.03.007>
- Renner, J., Stöckhert, B., Zerbian, A., Röller, K., & Rummel, F. (2001). An experimental study into the rheology of synthetic polycrystalline coesite aggregates. *Journal of Geophysical Research*, 106(B9), 19,411–19,429. <https://doi.org/10.1029/2001JB000431>
- Rubie, D. C., Karato, S., Yan, H., & O'Neill, H. S. C. (1993). Low differential stress and controlled chemical environment in multianvil high-pressure experiments. *Physics and Chemistry of Minerals*, 20(5), 315–322. <https://doi.org/10.1007/BF00215102>
- Rutter, E., & Brodie, K. (2004). Experimental intracrystalline plastic flow in hot-pressed synthetic quartzite prepared from Brazilian quartz crystals. *Journal of Structural Geology*, 26(2), 259–270. [https://doi.org/10.1016/S0191-8141\(03\)00,096-000988](https://doi.org/10.1016/S0191-8141(03)00,096-000988)
- Shatskiy, A., Yamazaki, D., Borzdov, Y. M., Matsuzaki, T., Litasov, K. D., Cooray, T., et al. (2010). Stishovite single-crystal growth and application to silicon self-diffusion measurements. *American Mineralogist*, 95(1), 135–143. <https://doi.org/10.2138/am.2010.3255>
- Shelton, G., & Tullis, J. (1981). Experimental flow laws for crustal rocks. *Eos, Transactions American Geophysical Union*, 62, 396.
- Singh, A. K., Andrault, D., & Bouvier, P. (2012). X-ray diffraction from stishovite under nonhydrostatic compression to 70 GPa: Strength and elasticity across the tetragonal→orthorhombic transition. *Physics of the Earth and Planetary Interiors*, 208–209, 1–10. <https://doi.org/10.1016/j.pepi.2012.07.003>
- Singh, A. K., Balasingh, C., Mao, H., Hemley, R. J., & Shu, J. (1998). Analysis of lattice strains measured under nonhydrostatic pressure. *Journal of Applied Physics*, 83(12), 7567–7575. <https://doi.org/10.1063/1.367872>
- Sugahara, M., Yoshiasa, A., Komatsu, Y., Yamanaka, T., Bolfan-Casanova, N., Nakatsuka, A., et al. (2006). Reinvestigation of the MgSiO<sub>3</sub> perovskite structure at high pressure. *American Mineralogist*, 91(4), 533–536. <https://doi.org/10.2138/am.2006.1980>
- Tamura, N. (2014). XMAS: A versatile tool for analyzing synchrotron X-ray microdiffraction data. In *Strain and Dislocation Gradients from Diffraction* (pp. 125–155). London UK: Imperial College Press. [https://doi.org/10.1142/9781908979636\\_0004](https://doi.org/10.1142/9781908979636_0004)
- Texier, M., & Cordier, P. (2006). TEM characterization of dislocations and slip systems in stishovite deformed at 14 GPa, 1,300°C in the multianvil apparatus. *Physics and Chemistry of Minerals*, 33(6), 394–402. <https://doi.org/10.1007/s00269-006-0088-8>
- Thomson, A. R., Kohn, S. C., Bulanova, G. P., Smith, C. B., Araujo, D., EIMF, & Walter, M. J. (2014). Origin of sub-lithospheric diamonds from the Juina-5 kimberlite (Brazil): Constraints from carbon isotopes and inclusion compositions. *Contributions to Mineralogy and Petrology*, 168(6). <https://doi.org/10.1007/s00410-014-1081-8>
- Tsujino, N., Nishihara, Y., Yamazaki, D., Seto, Y., Higo, Y., & Takahashi, E. (2016). Mantle dynamics inferred from the crystallographic preferred orientation of bridgmanite. *Nature*, 539(7627), 81–84. <https://doi.org/10.1038/nature19777>
- Van Huffel, S., & Vandewalle, J. (1989). On the accuracy of total least squares and least squares techniques in the presence of errors on all data. *Automatica*, 25(5), 765–769. [https://doi.org/10.1016/0005-1098\(89\)90033-2](https://doi.org/10.1016/0005-1098(89)90033-2)
- Wang, Z., Zhao, Y., & Kohlstedt, D. L. (2010). Dislocation creep accommodated by grain boundary sliding in dunite. *Journal of Earth Science*, 21(5), 541–554. <https://doi.org/10.1007/s12583-010-0113-1>
- Warren, J. M., & Hirth, G. (2006). Grain size sensitive deformation mechanisms in naturally deformed peridotites. *Earth and Planetary Science Letters*, 248(1–2), 438–450. <https://doi.org/10.1016/j.epsl.2006.06.006>
- Wu, M., Liang, Y., Jiang, J., & Tse, J. (2012). Structure and properties of dense silica glass. *Scientific Reports*, 2(1). <https://doi.org/10.1038/srep00398>
- Xiao, X., Wirth, R., & Dresen, G. (2002). Diffusion creep of anorthite-quartz aggregates. *Journal of Geophysical Research*, 107(B11), 2279. <https://doi.org/10.1029/2001JB000789>
- Xu, F., Yamazaki, D., Sakamoto, N., Sun, W., Fei, H., & Yurimoto, H. (2017). Silicon and oxygen self-diffusion in stishovite: Implications for stability of SiO<sub>2</sub>-rich seismic reflectors in the mid-mantle. *Earth and Planetary Science Letters*, 459, 332–339. <https://doi.org/10.1016/j.epsl.2016.11.044>
- Yamazaki, D., Kato, T., Yurimoto, H., Ohtani, E., & Toriumi, M. (2000). Silicon self-diffusion in MgSiO<sub>3</sub> perovskite at 25 GPa. *Physics of the Earth and Planetary Interiors*, 119(3–4), 299–309. [https://doi.org/10.1016/S0031-9201\(00\)00135-7](https://doi.org/10.1016/S0031-9201(00)00135-7)
- Zedgenizov, D. A., Shatsky, V. S., Panin, A. V., Evtushenko, O. V., Ragozin, A. L., & Kagi, H. (2015). Evidence for phase transitions in mineral inclusions in superdeep diamonds of the Sao Luiz deposit (Brazil). *Russian Geology and Geophysics*, 56(1–2), 296–305. <https://doi.org/10.1016/j.rgg.2015.01.021>
- Zhang, J., Liebermann, R., Gasparik, T., Herzberg, C., & Fei, Y. (1993). Melting and subsolidus relations of SiO<sub>2</sub> at 9–14 GPa. *Journal of Geophysical Research*, 98(B11), 19,785–19,793. <https://doi.org/10.1029/93JB02218>